

# Influence of the loading path on fatigue crack growth under mixed-mode loading

V. Doquet · M. Abbadi · Q. H. Bui · A. Pons

Received: 24 April 2009 / Accepted: 2 September 2009  
© Springer Science+Business Media B.V. 2009

**Abstract** Fatigue crack growth tests were performed under various mixed-mode loading paths, on maraging steel. The effective loading paths were computed by finite element simulations, in which asperity-induced crack closure and friction were modelled. Application of fatigue criteria for tension or shear-dominated failure after elastic–plastic computations of stresses and strains, ahead of the crack tip, yielded predictions of the crack paths, assuming that the crack would propagate in the direction which maximises its growth rate. This approach appears successful in most cases considered herein.

**Keywords** Mixed-mode · Non-proportional loading · Fatigue crack · Bifurcation

## 1 Introduction

Under non-proportional cyclic loading, the stress or strain ranges were shown not to be sufficient to model the multiaxial cyclic behaviour of metals (Benallal and Marquis 1987; Doquet and Pineau 1990; Feaugas and Clavel 1997) and parameters describing the loading path had to be introduced into constitutive equations to capture extra-hardening or softening effects

(Benallal and Marquis 1987). Concerning fatigue crack growth under non-proportional mixed-mode, a similar question arises: are  $\Delta K_I$ ,  $\Delta K_{II}$  (or  $\Delta K_{III}$ ) and R ratios sufficient to predict crack paths and growth rates? Does the loading path have an intrinsic influence, or can all this influence be captured through appropriate corrections for closure and friction effects on stress intensity factors, that is, by the use of  $\Delta K_I^{\text{effective}}$ ,  $\Delta K_{II}^{\text{effective}}$ ,  $\Delta K_{III}^{\text{effective}}$ ?

This problem is complex and no clear answer emerges from the literature on non-proportional mixed-mode I and II (Gao et al. 1983; Hourlier et al. 1985; Wong et al. 1996, 2000; Planck and Kuhn 1999; Yu and Abel 2000; Doquet and Pommier 2004) or mode I and III (Feng et al. 2006). The latter concludes: “with identical loading magnitudes in the axial and torsional directions, the crack growth and crack profiles are strongly dependent on the loading path. The observed results create a great challenge to the crack growth theories for general loading conditions”.

At least three types of interactions between mode I and mode II can be distinguished.

### 1.1 Kinematic interactions between the crack faces

Mode I reduces crack faces contact and friction and thus tends to increase  $\Delta K_{II}^{\text{effective}}$  (Yu and Abel 1999), whereas static or intermittent mode II produces a relative shift of the crack faces thus increasing asperity-induced closure and reducing  $\Delta K_I^{\text{effective}}$  (Stanzl et al. 1989; Dahlin and Olsson 2003). But, on the other

V. Doquet (✉) · M. Abbadi · Q. H. Bui · A. Pons  
Laboratoire de Mécanique des Solides, Ecole  
Polytechnique, CNRS, Palaiseau cedex 91128, France  
e-mail: doquet@lms.polytechnique.fr  
URL: <http://www.lms.polytechnique.fr>

hand, pure mode II loading on a rough crack generates a cyclic mode I, because gliding asperities wedge the crack open. Several analytical models (Tong et al. 1995; Yu and Abel 1999; Bian et al. 2006) were developed to describe the latter effect, but the assumption of rigid asperities leads to overestimate the induced  $K_I$  and to underestimate  $\Delta K_{II}^{\text{effective}}$ . Elastic–plastic finite element simulations taking into account the contact and friction of crack face asperities can be used to overcome this limitation, as shown below.

On the other hand, shear-mode loading superimposed on mode I may have an indirect influence on plasticity-induced closure, because it modifies the plastic flow at the crack tip.

### 1.2 Plastic interactions

Plastic interactions concern plastic flow ahead of the crack tip. An example is given on Fig. 1a. Considering the yield surface and plastic flow of the material ahead of the crack tip, a static tensile stress along the ligament due to applied mode I should lower the yield stress in shear and thus enhance cyclic shear-mode plasticity. This is confirmed by the finite element computations of the shear strain range ahead of the crack tip, shown on Fig. 1b. It should also promote tensile plastic flow and ratchetting, at least for a transient period (i.e. until the center of the yield surface has been shifted to point E by kinematic hardening). This may cause an *intrinsic* acceleration of mode II crack growth, that is: not due to an increase in  $\Delta K_{II}^{\text{effective}}$ . Similarly, an applied shear stress associated to present or past mode II loading can enhance tensile plastic flow compared to pure mode I. Similar effects were also shown to occur due to residual tensile or shear stresses, in sequential mixed-mode loading (Doquet and Pommier 2004). The latter effect might thus also increase plasticity-induced closure.

A possible influence of non-proportional loading ahead of the crack tip on the constitutive equations of the material—extra cyclic hardening in some single-phase alloys (Benallal and Marquis 1987; Doquet and Pineau 1990), or extra cyclic softening in some titanium alloys (Feaugas and Clavel 1997)—also has to be kept in mind.

### 1.3 Damage interactions

Damage interactions concern fatigue damage ahead of the crack tip. Gao et al. (1983) argue that since

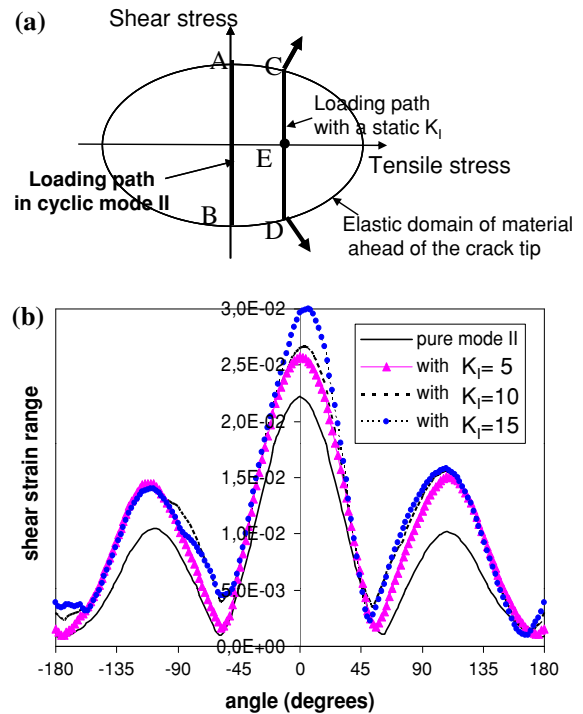


**Fig. 1** Illustrations of “plastic interactions” between mode I and mode II. **a** Schematic loading path, initial yield domain (Von Mises criterion) and plastic flow for a small volume element at a crack tip loaded either in reversed mode II or reversed mode II + static mode I. The shift of the yield surface in the direction of plastic flow due to kinematic hardening at point C and D has not been represented, for sake of clarity. **b** Angular distribution of the shear strain range  $20\mu\text{m}$  ahead of the crack tip, computed by FEM, for reversed mode II,  $\Delta K_{II} = 20\text{MPa}\sqrt{\text{m}}$ , with various static  $K_I$ , in maraging steel

dislocation glide and damage induced by non-proportional mixed-mode loading ahead of a crack tip are distributed over a wide range of slip planes orientation, whereas it is concentrated, under proportional loading, the plastic strain in the maximum shear direction will be lower in the first case, for equivalent  $\Delta K_I$ ,  $\Delta K_{II}$ , so that the crack growth rate would be intrinsically lower under non-proportional loading.

However, it is generally accepted that shear-initiated decohesion along a slip band in fatigue is triggered by an opening stress and that the presence of an opening stress can—to a certain degree—compensate a reduction in shear stress or strain range.

Findley (1957) took this effect into account in a crack initiation criterion where the damage function:

$$\beta_{\text{Find}} = \Delta\tau + k\sigma_{n,\text{max}} \quad (1)$$

includes the peak opening stress  $\sigma_{n,\max}$ , computed along the facet which undergoes the maximum shear stress range,  $\Delta\tau$ . The constant  $k$  determines the “weight” of the tensile stress for the material of interest. If mode II fatigue crack growth—observed when  $\Delta K_{II}^{\text{effective}}$  is above a material-dependent threshold—is due to shear-initiated fatigue fracture of grains located in the crack plane ahead of the tip, then, according to Eq. 1, this fracture should occur earlier when an opening stress due mode I loading is present, and lead to faster crack growth, if no bifurcation occurs.

The relative importance of these three types of interactions is likely to depend on the microstructure, and mechanical properties of the material, as well as on the loading conditions: R ratio, frequency and environment. A coarse microstructure, a high friction coefficient, or a small or negative mode I R ratio should promote kinematic interactions, while the importance of plastic interactions should depend on the yield stress and type of hardening i.e. isotropic, linear or non linear kinematic hardening. The importance of damage interactions should be higher in materials which exhibit a substantial difference in their fatigue resistance in push–pull and torsion (which results in a high value of the coefficient  $k$  in Eq. 1).

The present investigation is based on crack growth tests under various mixed-mode loading paths on maraging steel and observation of crack paths and growth rates. It also includes elastic–plastic finite element simulations in which asperity-induced closure and friction are modeled. It provides some elements about these three types of interactions. Moreover, application of fatigue criteria for tension or shear-dominated failure after elastic–plastic computations of stresses and strains cycles, ahead of the crack tip—assuming that the crack propagates in the direction which maximises its growth rate—yields predictions of the crack paths and growth rates that correspond well to experimental observations.

## 2 Experiments

### 2.1 Procedures

The material investigated is a maraging steel (Z2NKD 18-8-5), for which kinetic data concerning mode II fatigue crack growth are available from a previous study (Pinna and Doquet 1999). It has a very high

yield stress ( $R_{p0.2} \approx 1720$  MPa) but very low hardening capacity ( $R_m/R_{p0.2} \approx 1.03$ ) and limited ductility (around 8%). Tubular specimens (10.8 and 9 mm outer and inner diameters) were used for push–pull, reversed torsion and reversed torsion plus static tension tests, in order to fit constitutive equations and two fatigue criteria: one for shear-dominated failure—which occurred systematically in torsion—(Findley’s criterion (Findley 1957)) and one for tension-dominated failure which occurred in push–pull (Smith, Watson and Topper’s criterion (Smith et al. 1970)). This preliminary part of the study is reported in Appendix A.

Some tubular specimens had a circular hole (370  $\mu\text{m}$  in diameter) from which a 1 to 1.5 mm-long transverse precrack was grown in mode I. Square shaped gold microgrids with a 4  $\mu\text{m}$  pitch were laid on some specimens, along the precrack plane. The grids were used to measure crack face relative opening and sliding displacements by digital image correlation, using sequential SEM images taken during load cycles applied in situ by a tension–torsion machine (Bertolino and Doquet 2009).

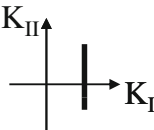
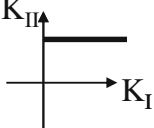
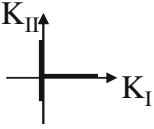
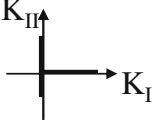
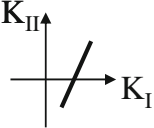
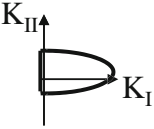
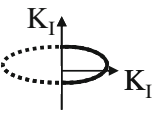
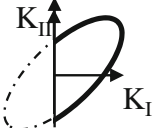
The pre-cracked specimens were submitted to tension and torsion cyclic loadings, following various loading paths (Table 1). These loadings included various blocks with constant nominal  $\Delta K_I$  and  $\Delta K_{II}$  or constant static  $K_I$  or  $K_{II}$ . Loading E and F, which both appear as truncated ellipses in  $K_I - K_{II}$  plane, correspond to 90° out-of-phase tension and shear, but in the first case, loading is fully reversed, while in the second case, only shear-mode loading is reversed, but  $R=0$  for mode I. Loading G, represented as an inclined truncated ellipse in  $K_I - K_{II}$  plane corresponds to 30° out-of-phase push–pull and torsion.

### 2.2 Nominal and effective loading paths

$K_I^{\text{nominal}}$ ,  $K_{II}^{\text{nominal}}$  were computed for a crack emanating from a hole in a infinite plate, but corrections were applied to take into account the influence of the curvature of the tube wall, which, according to Erdogan and Ratwani (1972) increases as the crack grows.

Two-dimensional plane stress finite element simulations of applied loadings were performed with rough crack faces (Fig. 2), taking into account the contact and friction of the asperities, according to Coulomb’s law. The Cast3M code was used, with nearly 40,000 four nodes quadrangular and three nodes triangular

**Table 1** Loading parameters and bifurcation angles

Loading path	ref	Loading parameters	Measured bifurcation angle	Predicted bifurcation angle
	A	$\Delta K_{II} = 20 \text{ MPa}\sqrt{\text{m}}$ , $K_I = 7.5 \text{ MPa}\sqrt{\text{m}}$ $\Delta K_{II} = 20 \text{ MPa}\sqrt{\text{m}}$ , $K_I = 10 \text{ MPa}\sqrt{\text{m}}$ $\Delta K_{II} = 20 \text{ MPa}\sqrt{\text{m}}$ , $K_I = 13 \text{ MPa}\sqrt{\text{m}}$	0 0 0	0 0 0
	B	$\Delta K_I = 15 \text{ MPa}\sqrt{\text{m}}$ , $K_{II} = 10 \text{ MPa}\sqrt{\text{m}}$	$< 4^\circ$	0
	C1	$\Delta K_I = 5.6 \text{ MPa}\sqrt{\text{m}}$ , $\Delta K_{II} = 20 \text{ MPa}\sqrt{\text{m}}$ $\Delta K_I = 11 \text{ MPa}\sqrt{\text{m}}$ , $\Delta K_{II} = 20 \text{ MPa}\sqrt{\text{m}}$ $\Delta K_I = 16.4 \text{ MPa}\sqrt{\text{m}}$ , $\Delta K_{II} = 20 \text{ MPa}\sqrt{\text{m}}$ $\Delta K_I = 21 \text{ MPa}\sqrt{\text{m}}$ , $\Delta K_{II} = 20 \text{ MPa}\sqrt{\text{m}}$ $\Delta K_I = 26 \text{ MPa}\sqrt{\text{m}}$ , $\Delta K_{II} = 20 \text{ MPa}\sqrt{\text{m}}$	0 0 0 0 $< 4^\circ$	0 0 0 0 0
	C2	$\Delta K_I = 16 \text{ MPa}\sqrt{\text{m}}$ , $\Delta K_{II} = 30 \text{ MPa}\sqrt{\text{m}}$ $\Delta K_I = 23.7 \text{ MPa}\sqrt{\text{m}}$ , $\Delta K_{II} = 30 \text{ MPa}\sqrt{\text{m}}$ $\Delta K_I = 32 \text{ MPa}\sqrt{\text{m}}$ , $\Delta K_{II} = 30 \text{ MPa}\sqrt{\text{m}}$	0 0 $< 4^\circ$	0 0 0
	D	$\Delta K_I = 10 \text{ MPa}\sqrt{\text{m}}$ , $\Delta K_{II} = 20 \text{ MPa}\sqrt{\text{m}}$	$0^\circ$ for $80\mu\text{m}$ then $30^\circ$	0
	E	$\Delta K_I = 7.5 \text{ MPa}\sqrt{\text{m}}$ , $\Delta K_{II} = 20 \text{ MPa}\sqrt{\text{m}}$ $\Delta K_I = 10 \text{ MPa}\sqrt{\text{m}}$ , $\Delta K_{II} = 20 \text{ MPa}\sqrt{\text{m}}$	0 0	0 0
	F	$\Delta K_I = 7.8 \text{ MPa}\sqrt{\text{m}}$ , $\Delta K_{II} = 20 \text{ MPa}\sqrt{\text{m}}$ $\Delta K_I = 10.6 \text{ MPa}\sqrt{\text{m}}$ , $\Delta K_{II} = 20 \text{ MPa}\sqrt{\text{m}}$ $\Delta K_I = 16 \text{ MPa}\sqrt{\text{m}}$ , $\Delta K_{II} = 20 \text{ MPa}\sqrt{\text{m}}$	0 0 50	0 0 0
	G	$\Delta K_I = 5.3 \text{ MPa}\sqrt{\text{m}}$ , $\Delta K_{II} = 10.6 \text{ MPa}\sqrt{\text{m}}$	38	54

**Fig. 2** Finite element model for the computation of effective loading paths. **a** Mesh and boundary conditions. **b, c** Deformed mesh for two levels of applied shear-mode loading. Asperities wedge the crack open

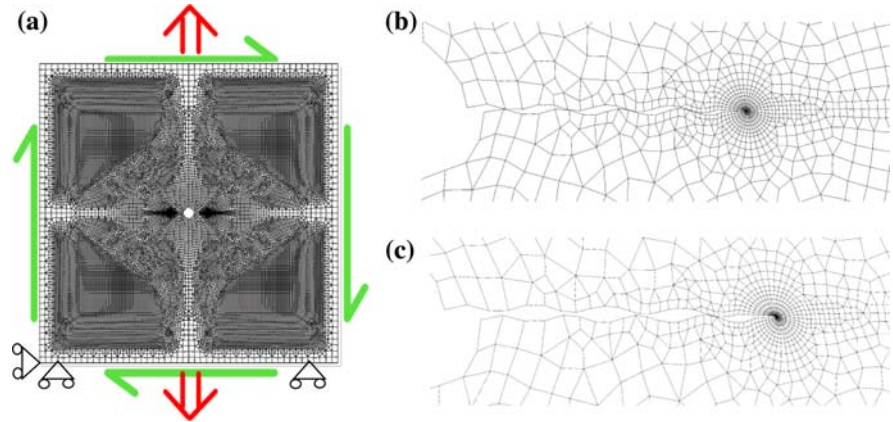
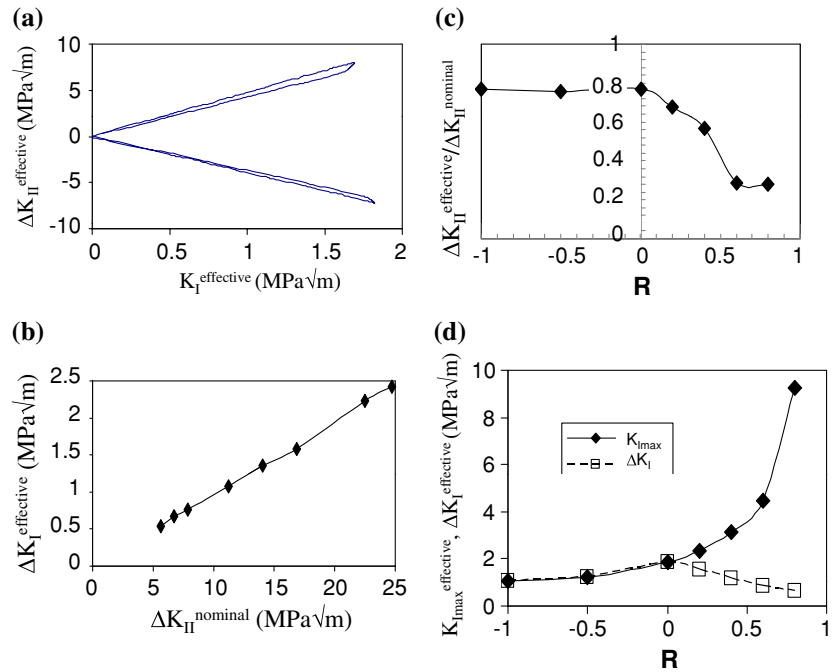


**Fig. 3** Outcome of finite element simulations of a rough crack loaded in mode II. **a** Effective loading path for  $R = -1$ , **b** asperity-induced  $\Delta K_I$  as a function of  $\Delta K_{II}^{nominal}$ , for  $R = -1$ , **c**  $\Delta K_{II}^{effective} / \Delta K_{II}^{nominal}$  as a function of  $R$ , **d** asperity-induced  $K_{I,max}$  and  $\Delta K_I$  as a function of  $R$



elements. A sinus profile with amplitude  $h$ —ranging from 5 to  $20\mu\text{m}$ —and period  $p$ —around  $180\mu\text{m}$ —was assumed, which is simplified, but reasonable compared to the observed precrack profiles.

The effective stress intensity factors,  $K_{II}^{effective}$ ,  $K_{I}^{effective}$ , were computed at each time step (by analysis of crack faces displacements). Plasticity-induced closure—probably limited in such a high-strength steel—was not taken into account.

Simulations of pure mode II loading were performed for a rough crack, with  $h = 5, 10$  and  $15\mu\text{m}$  and friction coefficients,  $\mu$ , between 0 and 1, for  $\Delta K_{II}^{nominal}$  ranging from 5 to  $25\text{MPa}\sqrt{\text{m}}$  and  $R$  ratios from  $-1$

to 0.7. Figure 3a shows an example of computed effective loading path—which appears non-proportional—with some asperity-induced mode I, rising linearly with  $\Delta K_{II}^{nominal}$ , for a given crack roughness profile (Fig. 3b). The computed effective loading path is rather similar to that obtained with an analytical model—assuming rigid asperities—by Yu and Abel (1999).

$\Delta K_{II}^{effective} / \Delta K_{II}^{nominal}$  was found to be independent of  $\Delta K_{II}^{nominal}$  in the range simulated, but decreasing with  $R$ , when the latter is positive, as shown on Fig. 3c. This curve also is similar to that obtained by Yu and Abel and consistent with some experimental observations on Al alloys, by Planck and Kuhn (1999) who

**Fig. 4** Influence of crack roughness and friction coefficient on (a)  $\Delta K_I^{\text{effective}}$  and (b)  $\Delta K_{II}^{\text{effective}}$  in reversed mode II

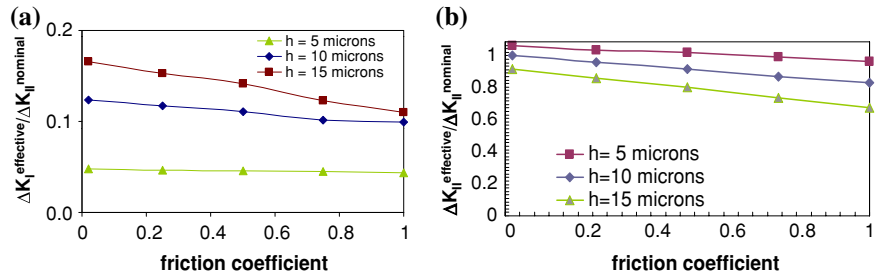


**Fig. 5** Computed evolutions of effective stress intensity factors: (a)  $K_I$  for loading B and (b)  $K_I$  and  $K_{II}$  for loading D

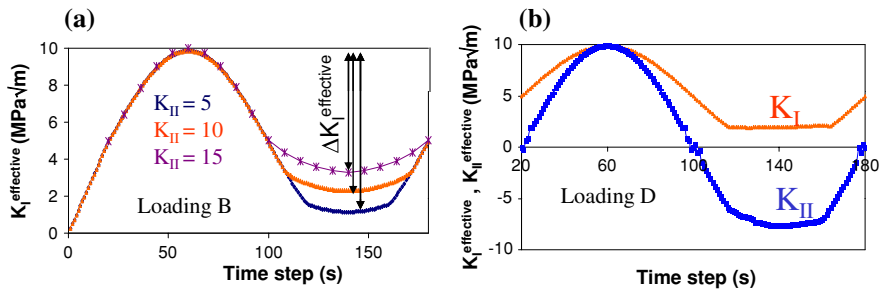
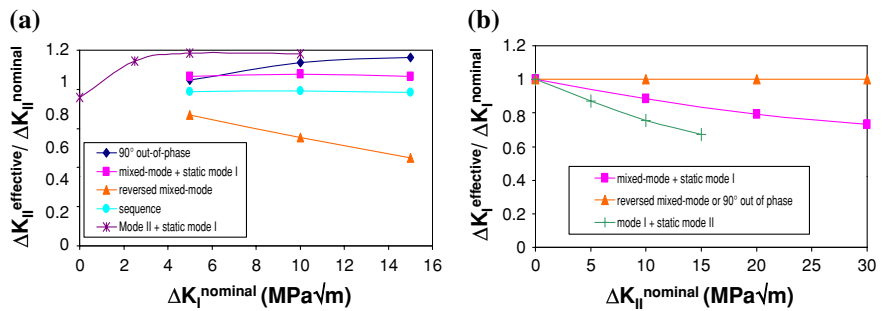


**Fig. 6** Mutual influence of mode I and mode II on the effective fraction of  $\Delta K$  of the other mode ( $h = 10\mu\text{m}$ ,  $p = 180\mu\text{m}$ ) (a)  $\Delta K_{II} = 20\text{MPa}\sqrt{\text{m}}$  and (b)  $\Delta K_I = 10\text{MPa}\sqrt{\text{m}}$



report no coplanar crack propagation for R values  $\geq 0.6$ , independently from  $\Delta K_{II}^{\text{nominal}}$ , while for lower R-ratios, mode II crack growth was observed, when  $\Delta K_{II}$  was high enough.

The plateau on this curve, as well as on the curve showing the asperity-induced  $K_I$  (Fig. 3d), for R between  $-1$  and  $0$  is also consistent with the absence of any measurable difference in mode II crack growth kinetics for  $R=0$  or  $R=-1$  reported by Otsuka et al. (1987) on Al alloys or Pinna and Doquet (1999) on maraging steel. Note that for  $R > 0$ , the maximum induced  $K_I$  is predicted to increase substantially, but the amplitude  $\Delta K_I$  to decrease.

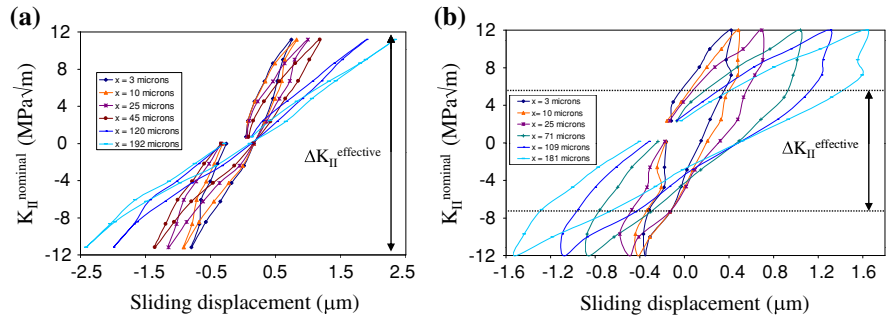
The higher the friction coefficient,  $\mu$ , the smaller the asperity-induced  $\Delta K_I$  and  $\Delta K_{II}^{\text{effective}}$  (Fig. 4). As it could be expected, Mode I induced by asperities is predicted to increase and  $\Delta K_{II}^{\text{effective}}$  to decrease with the height  $h$  of the asperities.

Figure 5 shows the evolutions in time of effective stress intensity factors computed for loading B (cyclic mode I plus static mode II) and D (in-phase mixed-mode plus static mode I), with  $h = 10\mu\text{m}$  and friction coefficient  $\mu = 1$ . Important asperity-induced closure—increasing with  $K_{II}$ —was found for cyclic mode I plus static mode II. Closure effects were found less important for mixed-mode plus static mode I and absent for all other investigated loading paths. Figure 6 shows the mutual influence of each mode on the effective stress intensity factor of the other mode for  $\Delta K_I = 10\text{MPa}\sqrt{\text{m}}$  and  $\Delta K_{II} = 20\text{MPa}\sqrt{\text{m}}$ .

A static mode I was found to reduce or even suppress crack faces interactions and to increase  $\Delta K_{II}^{\text{effective}}$ . For  $h = 10\mu\text{m}$  and  $\mu = 1$ ,  $K_I = 5\text{MPa}\sqrt{\text{m}}$  is predicted to be sufficient for  $\Delta K_{II}^{\text{effective}}$  to reach  $\Delta K_{II}^{\text{nominal}}$ . This is consistent with the measured load-sliding displacement loops measured in the SEM, at various distance behind



**Fig. 7** Nominal  $K_{II}$  versus sliding displacement measured by SEM digital image correlation at various distance behind the crack tip for (a) pure reversed mode II and (b) reversed mode II + static  $K_I = 7.5 \text{ MPa } \sqrt{\text{m}}$



the crack tip, using digital image correlation (Fig. 7). Figure 7a, obtained in pure mode II, shows vertical segments—denoting a variation in  $K_{II}$  without sliding of the crack locked by asperities and friction—after each reversal. The effective part of the cycle—i.e. the part during which sliding occurs—can be deduced from these loops and  $\Delta K_{II}^{\text{effective}}$  evaluated as  $15 \text{ MPa } \sqrt{\text{m}}$ . By contrast, the loops of Fig. 7b, obtained with the same  $\Delta K_{II}^{\text{nominal}} = 21 \text{ MPa } \sqrt{\text{m}}$  but with a superimposed static  $K_I = 7.5 \text{ MPa } \sqrt{\text{m}}$  do not exhibit such vertical segments, which indicates that  $\Delta K_{II}^{\text{effective}} = \Delta K_{II}^{\text{nominal}}$ .

In-phase push-pull and reversed shear ( $R = -1$ ) was found to enhance crack faces interactions and to reduce  $\Delta K_{II}^{\text{effective}}$ , compared to pure mode II ( $\Delta K_{II}^{\text{effective}} = 11.4 \text{ MPa } \sqrt{\text{m}}$  for  $\Delta K_{II} = 20 \text{ MPa } \sqrt{\text{m}}$  and  $\Delta K_I = 10 \text{ MPa } \sqrt{\text{m}}$ ).

By contrast, out-of-phase push-pull and shear was also found to reduce crack faces interactions and to increase  $\Delta K_{II}^{\text{effective}}$  compared to in-phase push-pull or pure mode II, but to a lesser extent than a static  $K_I$ . Figure 8 shows the computed evolution of  $\Delta K_{II}^{\text{effective}} / \Delta K_{II}^{\text{nominal}}$  and effective R ratio for mode II (that is:  $R = K_{II\text{max}}^{\text{effective}} / K_{II\text{min}}^{\text{effective}}$ ) with the phase angle for  $\Delta K_{II} = 20 \text{ MPa } \sqrt{\text{m}}$ ,  $\Delta K_I = 5$  or  $10 \text{ MPa } \sqrt{\text{m}}$ ,  $h = 10 \mu\text{m}$  and  $\mu = 1$ . As the phase angle increases from 0 to  $90^\circ$ , the tensile part of the cycle provides less and less assistance to the forward slip of crack faces, but the compressive stage provides less and less resistance to their backward slip. This results in an increase of  $\Delta K_{II}^{\text{effective}}$  and a decrease of the effective mode II R ratio. By contrast,  $\Delta K_I^{\text{effective}} \approx \Delta K_I^{\text{nominal}}$  for any phase angle.

Very limited influence of mode I on  $\Delta K_{II}^{\text{effective}}$  was found here for sequential loading, but simulations performed for  $\Delta K_I = 15 \text{ MPa } \sqrt{\text{m}}$ ,  $\Delta K_{II} = 20 \text{ MPa } \sqrt{\text{m}}$  for a much softer ferritic-pearlitic steel in a previous

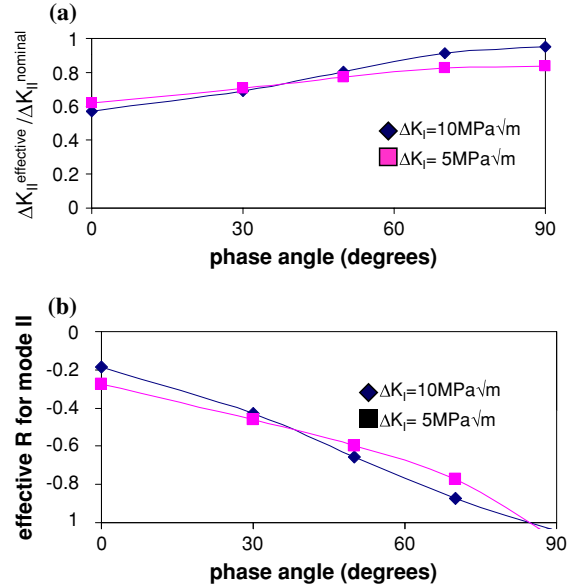


**Fig. 8** Computed evolution of (a)  $\Delta K_{II}^{\text{effective}} / \Delta K_{II}^{\text{nominal}}$  and (b) effective R ratio for mode II with the phase angle, for out-of-phase push-pull and reversed torsion, for  $\Delta K_{II} = 20 \text{ MPa } \sqrt{\text{m}}$ ,  $h = 10 \mu\text{m}$ ,  $p = 180 \mu\text{m}$

study (Pinna and Doquet 1999) have shown that for such loading, the residual crack tip opening increases from cycle to cycle. This effect, which would probably be observed in maraging steel at higher  $\Delta K_I$  is likely to reduce crack faces interference and increase  $\Delta K_{II}^{\text{effective}}$ .

Note that for similar nominal loading ranges,  $\Delta K_I = 10 \text{ MPa } \sqrt{\text{m}}$  and  $\Delta K_{II} = 20 \text{ MPa } \sqrt{\text{m}}$ , variations in the loading path lead to variations in  $\Delta K_I^{\text{effective}}$  from 7.9 (path B) to  $10 \text{ MPa } \sqrt{\text{m}}$  (path E or F) and in  $\Delta K_{II}^{\text{effective}}$  from 11.4 (path D) to  $20 \text{ MPa } \sqrt{\text{m}}$  (path A)! Such large differences in effective loading are likely to produce differences in crack paths and growth rates.

### 2.3 Observations

Table 1 summarises the observations, concerning the crack paths. Pictures of crack paths after loading C<sub>1</sub>, D and F are shown on Fig. 9.

Coplanar growth over more than 700 μm was observed for loading A—reversed mode II, with  $\Delta K_{II} = 20 \text{ MPa } \sqrt{\text{m}}$  and an increasing static K<sub>I</sub>. No deceleration was observed, contrary to what would happen in pure mode II, for the same  $\Delta K_{II}^{\text{nominal}}$  (Pinna and Doquet 1999). This is partly due to a higher  $\Delta K_{II}^{\text{effective}}$ , since it was shown above that K<sub>I</sub> = 7.5 MPa  $\sqrt{\text{m}}$  is enough to suppress crack face interference. But this acceleration of shear-mode crack growth by a static mode I cannot be reduced to a K<sub>I</sub>-induced increase in  $\Delta K_{II}^{\text{effective}}$  since compared to the growth rate for pure mode II with  $\Delta K_{II}^{\text{effective}} = 20 \text{ MPa } \sqrt{\text{m}}$  deduced from an interpolation of Pinna's data (Pinna and Doquet 1999), the growth rate measured during the first block, with the smallest K<sub>I</sub> is already five times higher and even increases slightly with K<sub>I</sub> : 8.2510<sup>-7</sup>, 8.6810<sup>-7</sup> and 8.7410<sup>-7</sup> respectively, for K<sub>I</sub> = 7.5, 10 and 13 MPa  $\sqrt{\text{m}}$ .

This effect can thus be attributed to a large extent to plastic and damage interaction ahead of the crack tip.

For loading B—cyclic mode I plus static mode II—the crack deviation did not exceed 4° and the growth rate was not significantly different from the growth rate measured for the same  $\Delta K_I$  during precracking in pure mode I.

Crack growth was nearly coplanar for sequential loadings C<sub>1</sub> and C<sub>2</sub>. The slight deflections observed during the final blocks of these tests seem not to be due to the applied mixed-mode, but to incipient shear-lips, due to the relatively high  $\Delta K_I$ . Figure 10 shows the evolution of measured coplanar crack growth rates with  $\Delta K_I$  for test C<sub>1</sub> and C<sub>2</sub>. For such sequential loading, it may seem reasonable to predict the coplanar crack growth rate by a simple sum:

$$\frac{da}{dN}(\text{sequence}) \approx \frac{da}{dN}(\Delta K_I^{\text{effective}}) + \frac{da}{dN}(\Delta K_{II}^{\text{effective}}) \quad (2)$$

Those predictions—based on the values of  $\Delta K_I^{\text{effective}}$  and  $\Delta K_{II}^{\text{effective}}$  computed for sequential loading with  $h = 10 \mu\text{m}$  and  $\mu = 1$  and the experimental mode I and mode II Paris laws—are plotted for comparison on Fig. 10. Equation 2 appears to underestimate the

measured crack growth rates by a factor of 3 to 5.5. A similar synergetic effect was reported in Wong et al. (1996, 2000) and Doquet and Pommier (2004) for rail steel.

Loading D—in phase mixed-mode plus static mode I—produced 80 μm coplanar crack growth, followed by bifurcation at 30°.

Coplanar crack growth was observed for path E (90° out-of-phase, but R=0 for mode I) and during the first and second block of fully reversed, 90° out-of-phase loading F. Bifurcation at 50° occurred during the third block. For loading F, a large quantity of fretting debris appeared along the rough precrack, but much less along the smoother coplanar crack part, grown in mixed-mode. Much less fretting debris was formed for path E and the fracture surfaces were not mated, contrary to the previous case.

Loading G—fully reversed, 30° out-of-phase push-pull and torsion—led to bifurcation at 38°. The crack was covered by fretting debris that had to be removed to allow observations.

These fretting debris are thus specially abundant for mixed-mode loadings with a compressive stage while shearing is being applied.

### 3 Analysis

Elastic–plastic FE simulations of applied loadings were performed for rough crack faces, using constitutive equations with isotropic and non-linear kinematic hardening fitted to measured stress–strain curves (see appendix B). Findley's damage function was computed ahead of the crack tip and averaged along the radial segment of length  $l$  ( $l = 20 \mu\text{m}$  in the computations reported below) for which the shear stress range was maximum, whereas for the computation and averaging of Smith-Watson-Topper's damage function, two possible choices of critical plane were considered: the planes along which either the peak normal stress,  $\sigma_{n,\text{max}}$ , or the normal stress range  $\Delta\sigma_n$  were maximum. These two cases, which can yield very different predictions, as shown below, will be denoted by SWTa and SWTb. These two potential growth directions were considered by Hourlier et al. (1985) and Dahlin and Olsson (2003). The former concluded that the direction of maximum  $\Delta\sigma_n$  was more suitable for alloys showing a limited influence of the R ratio on their mode I kinetics, which is the case of the maraging steel investigated here ( $da/dN$



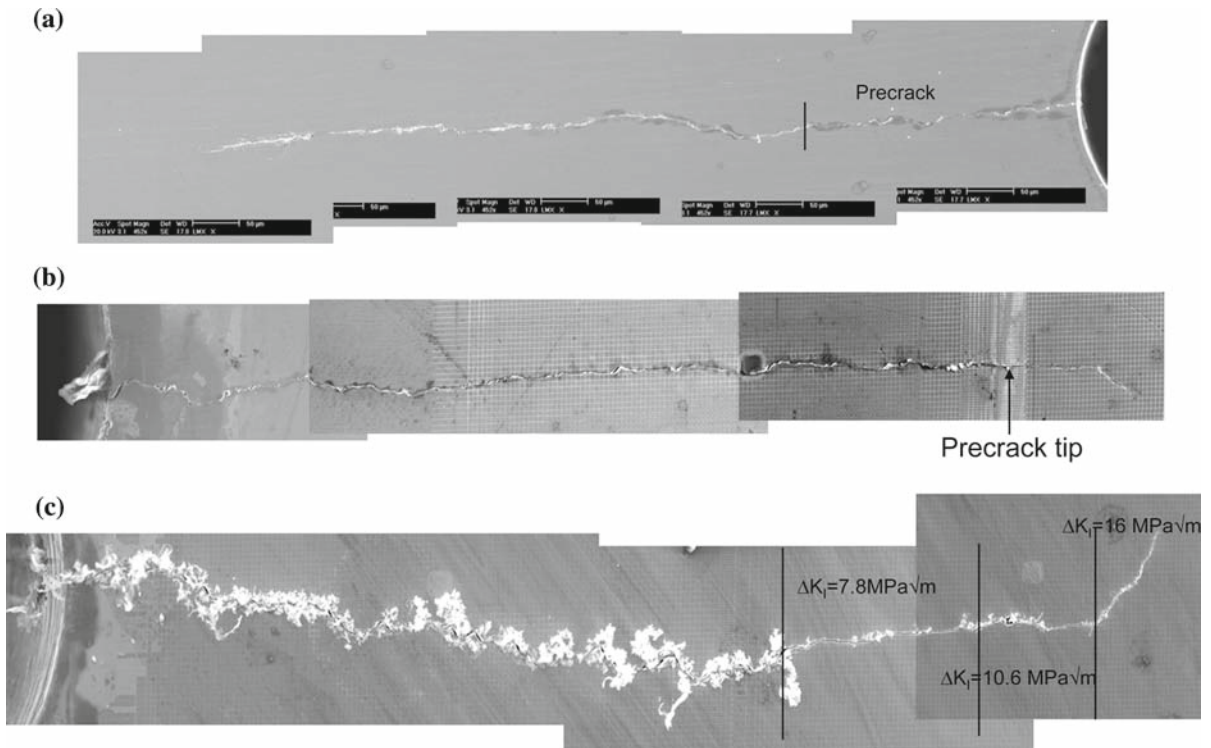
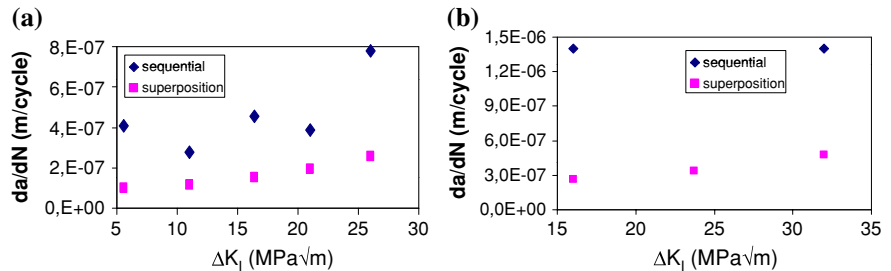


**Fig. 9** Crack paths for (a) sequential mixed-mode loading (C1) (b) in-phase mixed-mode + static mode I (D) (c) fully reversed 90° out-of-phase mixed-mode (F)

**Fig. 10** Evolution of coplanar crack growth rates with  $\Delta K_I$  in sequential loading for (a)  $\Delta K_{II} = 20 \text{ MPa}\sqrt{\text{m}}$  (test C1) and (b)  $\Delta K_{II} = 20 \text{ MPa}\sqrt{\text{m}}$  (test C2). Predictions based on a simple sum of crack growth rates in mode I and II are plotted for comparison



is at maximum 2.5 times higher for  $R=0.7$  than for  $R=0$ , for a given  $\Delta K_I$ ). The latter concluded that the direction of maximum  $\sigma_{n,max}$  should be preferred for high-strength metals with limited ductility, which is also the case of the maraging steel investigated here!

The analysis of the crack path for cyclic mode I + static mode II (test B) is very useful to solve that dilemma. For these loading conditions, the peak  $\sigma_{n,max}$  occurs at  $62^\circ$  while the maximum  $\Delta\sigma_n$  is at  $0^\circ$ , whatever the static mode is. Since no bifurcation occurred, the crack followed the maximum  $\Delta\sigma_n$  plane. Thus SWTb criterion was used for tension-dominated failure and Findley's criterion, for shear-dominated failure.

The potential numbers of cycles to failure  $N_f(l)$  are computed, using the analytical relations between damage functions and fatigue lives, fitted to experimental data on smooth specimens (see Appendix A). The crack is supposed to grow in the direction where failure—be it tension or shear-dominated—occurs first or, in other words, in the direction where its growth rate is maximum. It is consistent with experimental observations (Fig. 11) suggesting transient simultaneous coplanar growth and branch crack growth until the slowest crack gets arrested, due to increasing shielding by the other crack growing faster. It generalises the idea of Hourlier et al. (1985) who promoted it, under the

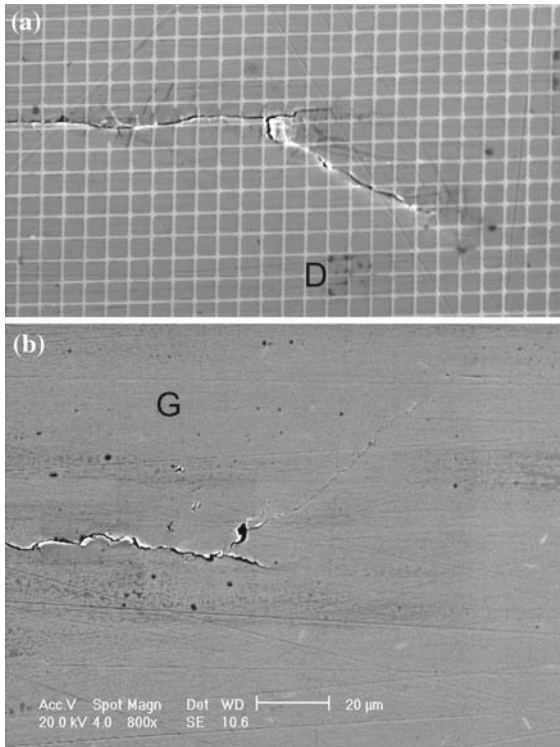


**Fig. 11** Zoom on the crack tips after loading D (a) and G (b) suggesting transient simultaneous coplanar growth and branch crack growth

restrictive assumption that mode I would necessary prevail. The potential growth rates in corresponding directions are then estimated as:

$$\frac{da}{dN} \approx \frac{l}{N_f(\ell)} \tag{3}$$

### 3.1 Prediction of crack path and growth rate under fully reversed mode II loading

Figure 12 compares the potential crack growth rate in fully reversed mode II predicted by Findley’s criterion and that of a branch crack, in mode I, according to SWTb for various amplitudes. These computations were performed for a smooth, frictionless crack. Coplanar growth is predicted for  $\Delta K_{II}^{effective}$  higher than 15 MPa  $\sqrt{m}$ , while bifurcation is predicted below this threshold value, which is consistent with the observations and measurements by Pinna and Doquet (1999). Most popular bifurcation criteria (based on the maximum tangential stress, minimum strain energy density, minimum radius of the plastic zone and many others)

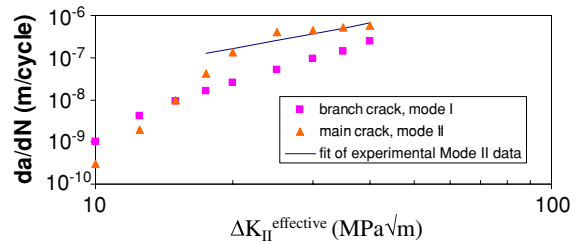


**Fig. 12** Potential crack growth rate in reversed mode II predicted by Findley’s criterion and that of a branch crack, in mode I, according to SWTb

would not predict this transition in the crack growth mode as  $\Delta K_{II}$  increases and would predict bifurcation whatever the loading range. The predicted mode II crack growth rate is correct above 25 MPa  $\sqrt{m}$ , but a bit too small below that value.

The computations of  $\Delta K_{II}^{effective}$  for reversed mode II on a rough crack reported on Fig. 4 show that  $\Delta K_{II}^{effective}$  decreases with  $h$  and  $\mu$ , so that for  $\Delta K_{II} = 20$  MPa  $\sqrt{m}$ , coplanar growth is predicted for  $h=5$  and  $10\mu m$ , whatever the friction coefficient, and for  $h=20\mu m$ , only if  $\mu$  is smaller than 0.44, while bifurcation is predicted above this value. Also,  $\Delta K_{II}^{effective}$  is predicted to decrease for positive R ratios (Fig. 3c), so that for  $\Delta K_{II} = 20$  MPa  $\sqrt{m}$ , coplanar growth is predicted from  $R = -1$  to 0 and bifurcation if  $R > 0$ .

Slight changes in crack roughness or tribological conditions are thus likely to change the crack paths. Mode II crack growth is favoured by smooth crack face, a low friction coefficient and reversed loading.

### 3.2 Prediction of crack paths in non-proportional mixed-mode

The predicted crack paths for mixed-mode loadings A to G reported in Table 1 were obtained for  $h = 10\mu m$  and  $\mu = 1$

#### 3.2.1 Reversed mode II plus static mode I

For loading A, coplanar crack growth is predicted, in accordance with the experiment. Figure 13 compares the predicted and measured coplanar crack growth rates for various static  $K_I$ , normalized by the growth rate in pure mode II, for  $\Delta K_{II}^{effective} = 20$  MPa  $\sqrt{m}$ . The order of magnitude of  $K_I$ -induced acceleration is well predicted, but tends to be exaggerated, as  $K_I$  increases.

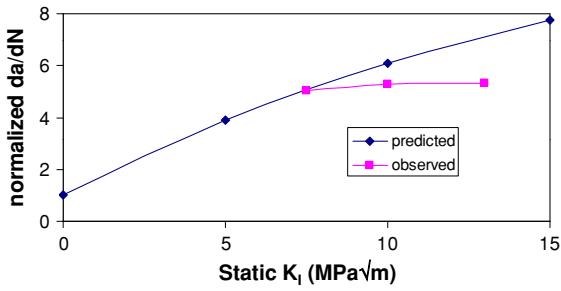


**Fig. 13** Comparison of predicted and measured influence of a static mode I on the coplanar crack growth rate, for  $\Delta K_{II}^{effective} = 20 \text{ MPa}\sqrt{\text{m}}$

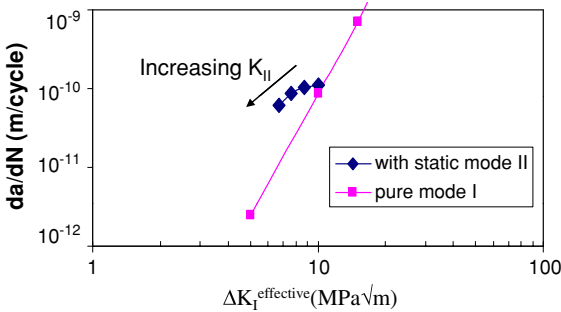


**Fig. 14** Influence of a static mode II on the coplanar crack growth rate in Mode I, as predicted by SWTb criterion

### 3.2.2 Cyclic mode I ( $R=0$ ) plus static mode II

As explained above, the SWTb criterion predicts coplanar growth in that case, in accordance with our observations during test B. The coplanar crack growth rate is predicted to decrease as the static  $K_{II}$  increases, due to asperity-induced decrease of  $\Delta K_I^{effective}$  (see Fig. 6a). However, as shown on Fig. 14, on which the computed growth rate is plotted versus  $\Delta K_I^{effective}$ , the deceleration is not as important as the decrease in  $\Delta K_I^{effective}$  would suggest: an intrinsic acceleration of crack growth by the static mode II is predicted. This is again an example of plastic interactions: an increase in the  $\Delta \epsilon_n$  term of the SWT criterion, caused by the static shear stress along the ligament associated with  $K_{II}$ .

It is in accordance with experimental results of Stanzl et al. (1989) who report, for 13Cr steel, mode I crack growth acceleration by a static mode II, for relatively short cracks (i.e. with few asperities) or after removal of asperities by a fine saw-cut, but deceleration for long cracks (many asperities, so that the  $K_{II}$ -

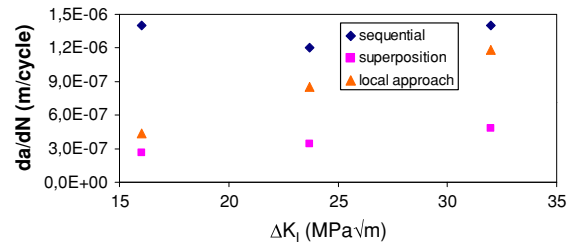


**Fig. 15** Improvement of the crack growth rate prediction by the local approach, for the sequential test C2, compared to a simple superposition (Eq. 1)

induced decrease in  $\Delta K_I^{effective}$  becomes predominant over the intrinsic acceleration). The observations made by You and Lee (1997) on a mild steel suggest the same effects: acceleration of mode I crack growth by a static mode II, if  $R > 0.2$  (no crack face interaction) but deceleration for lower R ratios.

### 3.2.3 Sequential mixed-mode loading

Coplanar growth is predicted for sequential loadings C1 and C2, in accordance with experimental observations. In addition, the local approach described above, which integrates both plastic and damage interactions improves the prediction of crack growth rates, as compared to the simple superposition of Eq. 2, as illustrated for test C2 on Fig. 15.

### 3.2.4 In-phase mixed-mode plus static mode I

For test D, the potential crack growth rates predicted by Findley and SWTb criteria are quite close, so that a slight change in crack roughness changes the predicted crack path: for  $h = 10\mu\text{m}$ , coplanar crack growth is predicted, while for  $h = 15\mu\text{m}$ , bifurcation should occur. The fact that coplanar growth was first observed over  $80\mu\text{m}$  before bifurcation might be the result of such an instable situation.

### 3.2.5 Out-of-phase mixed-mode loading

Simulations of out-of-phase push-pull and reversed torsion were performed for  $\Delta K_{II} = 10.6 \text{ MPa}\sqrt{\text{m}}$ ,  $\Delta K_I = 5.3 \text{ MPa}\sqrt{\text{m}}$  and for  $\Delta K_{II} = 20 \text{ MPa}\sqrt{\text{m}}$ ,  $\Delta K_I = 10 \text{ MPa}\sqrt{\text{m}}$ . Figure 16a and b compares the evolutions of predicted potential tensile and shear-mode crack growth rates with the phase angle and

Fig. 16c shows the corresponding bifurcation angles (similar for both amplitudes). For the smallest loading range, bifurcation in the direction experiencing maximum opening stress range is predicted, whatever the phase angle, with a bifurcation angle increasing from 54°, for in-phase loading, to 64° for 90° out-of-phase loading. Note that except for in-phase loading, the branch crack does not undergo pure mode I, since pure mode I or mode II do not exist when loading is non-proportional. For the highest loading range, a transition towards coplanar growth is predicted for 90° out-of-phase loading. These predictions are consistent with the results of test E ( $\Delta K_{II} = 20 \text{ MPa } \sqrt{\text{m}}$ ,  $\Delta K_I = 10 \text{ MPa } \sqrt{\text{m}}$ , 90° out-of-phase, coplanar growth) and G ( $\Delta K_{II} = 10.6 \text{ MPa } \sqrt{\text{m}}$ ,  $\Delta K_I = 5.3 \text{ MPa } \sqrt{\text{m}}$ , 30° out-of-phase, bifurcation). In the latter case, the measured bifurcation angle (38°) was however significantly smaller than predicted (54°).

Simulations were performed for  $\Delta K_{II} = 20 \text{ MPa } \sqrt{\text{m}}$  and  $\Delta K_I = 5, 10 \text{ or } 15 \text{ MPa } \sqrt{\text{m}}$  or path E (fully reversed), as well as for path F ( $R = 0$  for mode I). All of them predicted coplanar crack growth, with a growth rate increasing with  $\Delta K_I$ . The points corresponding to these computed growth rates fall near the predicted mode II kinetics on a  $da/dN$  versus  $\Delta K_{II}^{\text{effective}}$  plot. In that case, mode I is just predicted to increase  $\Delta K_{II}^{\text{effective}}$ , but not to trigger significantly damage ahead of the crack tip.

### 4 Conclusions

The “kinematic interactions” between mode I and II can be predicted by finite element simulations taking into account the contact and friction of crack face asperities. Such simulations show that for fixed nominal loading ranges, variations in the loading path induce important

**Fig. 16** Evolution with the phase angle of potential tensile and shear-mode crack growth rates, for out-of-phase push–pull and reversed torsion, computed with  $h = 10 \mu\text{m}$ ,  $p = 180 \mu\text{m}$  for (a)  $\Delta K_I = 5.3 \text{ MPa } \sqrt{\text{m}}$ ,  $\Delta K_{II} = 10.6 \text{ MPa } \sqrt{\text{m}}$  or (b)  $\Delta K_I = 10 \text{ MPa } \sqrt{\text{m}}$ ,  $\Delta K_{II} = 20 \text{ MPa } \sqrt{\text{m}}$  and (c) corresponding bifurcation angles

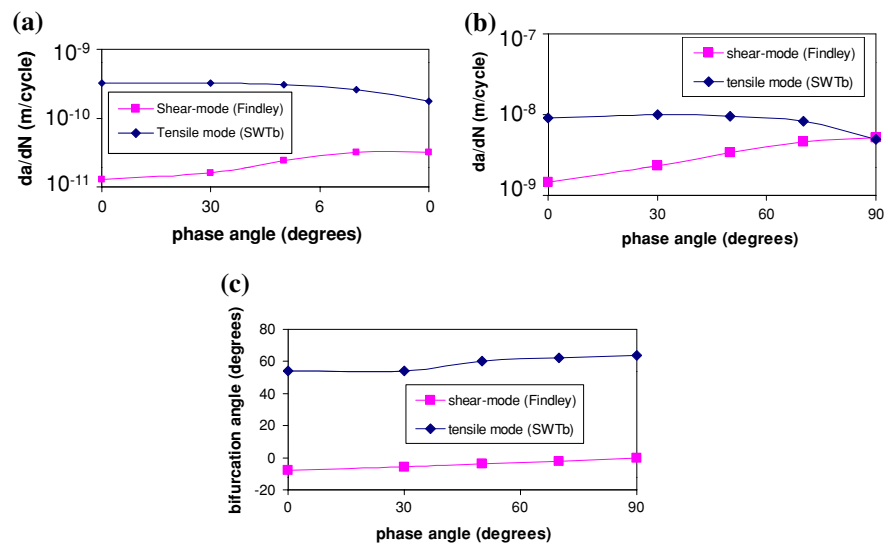


**Fig. 17** Fit of fatigue criteria

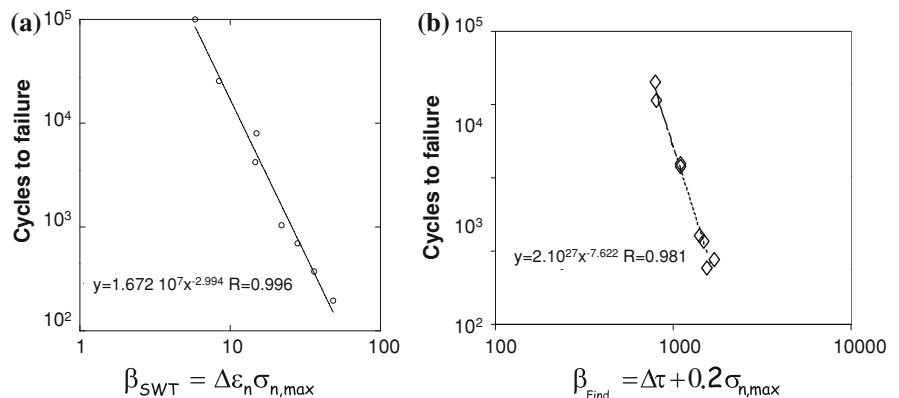
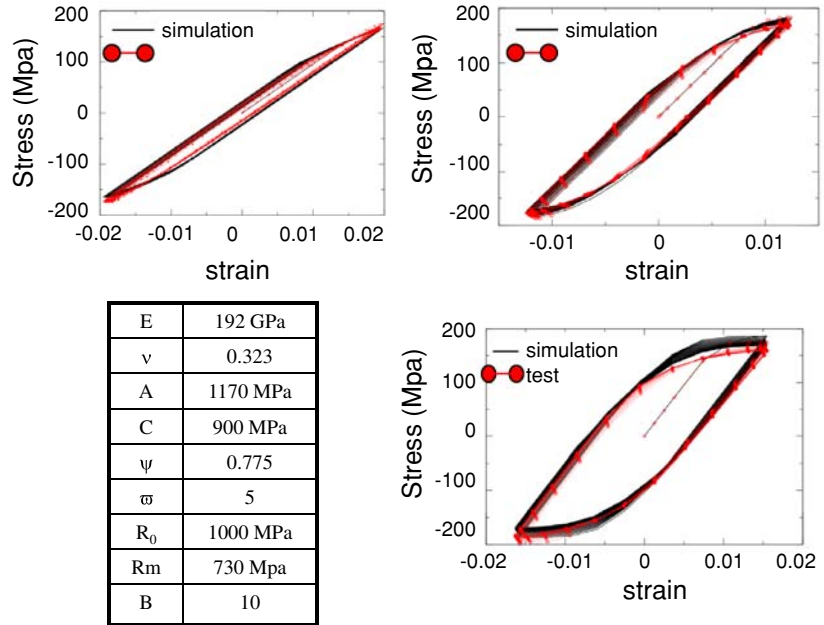


**Fig. 18** fit of constitutive equations



variations in  $\Delta K_I^{\text{effective}}$  and  $\Delta K_{II}^{\text{effective}}$  likely to change the crack path and growth rate.

However, linear elastic fracture mechanics parameters like  $\Delta K_I^{\text{effective}}$  and  $\Delta K_{II}^{\text{effective}}$  cannot represent the complex interaction of mode I and II in terms of crack tip plastic flow that is responsible for an intrinsic acceleration of mode II crack growth by a static mode I or of mode I crack growth by a static mode II.

In addition, for non-proportional loading, pure mode I or pure mode II crack growth do not exist: whatever the crack path, the crack is loaded in mixed-mode, so that the Paris laws for pure mode I or pure mode II are not appropriate to predict the growth rates.

For these reasons, an approach based on elastic–plastic FE computations and local application of fatigue criteria was preferred to analyze the crack paths observed during mixed-mode experiments on maraging steel. The predictions of crack paths were successful in most cases. Regarding the crack growth rates, the local approach performs better, for sequential loadings, than a simple superposition, which does not capture the observed synergetic interaction of mode I and II.

**Acknowledgment** This study was supported by the Agence Nationale de la Recherche.

### Appendix A: Fit of fatigue criteria

Tension-dominated failure which occurs in push–pull can be predicted with Smith, Watson and Topper’s criterion (Smith et al. 1970) in which the damage parameter is

$$\beta_{SWT} = \Delta \varepsilon_n \sigma_{n \max} \tag{4}$$

Figure 17a shows the measured fatigue lives in push–pull or repeated tension as a function of  $\beta_{SWT}$ . An exponential law was fitted and used for crack growth predictions.

Shear-initiated decohesion along a slip band in fatigue occurs earlier when an opening stress is present. Findley (1957) took this effect into account in a crack initiation criterion where the damage function:

$$\beta_{Find} = \Delta \tau + k \sigma_{n \max} \tag{5}$$

incorporates the peak opening stress  $\sigma_{n \max}$ , computed along the facet which undergoes the maximum shear stress range,  $\Delta \tau$ . Figure 17b shows the measured fatigue lives in reversed torsion with various static tensile stresses as a function of  $\beta_{SWT}$  in which  $k = 0.2$  gave the best correlation. There again an exponential fit was obtained.



## Appendix B: Fit of constitutive equations

Constitutive equations were fitted to some stress–strain curves obtained in push–pull, for which the material exhibits pronounced cyclic softening. A possible influence of non-proportional loading was not investigated. These equations—in which  $f$  denotes the yield function,  $J_2$  the second invariant of the stress deviator,  $p$  the cumulated equivalent plastic strain,  $\underline{X}$  and  $R$  kinematic and isotropic hardening variables and  $A$ ,  $C$ ,  $\psi$ ,  $\omega$ ,  $B$ ,  $R_0$ ,  $R_{\max}$ ,  $B$ , materials coefficients are:

$$f = J_2(\underline{\sigma} - \underline{X}) - R(p) \quad (6)$$

$$d\underline{X} = \frac{2}{3}CA [1 + (1 - \psi)e^{-\omega p}] \underline{d\varepsilon}_p - C\underline{X}dp \quad (7)$$

$$R = R_0 + (R_{\max} - R_0)(1 - e^{-Bp}) \quad (8)$$

$$dp = \sqrt{\frac{2}{3} \underline{d\varepsilon}_p : \underline{d\varepsilon}_p} \quad (9)$$

Figure 18 provides some examples of experimental and fitted stress–strain curves and the corresponding values of the material coefficients.

## References

- Benallal A, Marquis D (1987) Constitutive equations for nonproportional cyclic elastoviscoplasticity. *J Eng Mater Technol Trans* 109:326–336
- Bertolino G, Doquet V (2009) Derivation of effective stress intensity factors from measured crack face displacement. *Eng Fract Mech* 76:1574–1588
- Bian L-C, Fawaz Z, Behdinan K (2006) A mixed-mode crack growth model taking account of fracture surface contact and friction. *Int J Fracture* 139:39–58
- Dahlin P, Olsson M (2003) The effect of plasticity on incipient mixed-mode fatigue crack growth. *Fatigue Fract Eng Mater Struct* 26:577–588
- Doquet V, Pineau A (1990) Extra hardening due to cyclic non-proportional loading of an austenitic stainless steel. *Scripta Metallurgica* 24:433–438
- Doquet V, Pommier S (2004) Fatigue crack growth under non proportional mixed-mode loading in ferritic-pearlitic steel. *Fatigue Fract Eng Mater Struct* 27:1051–1060
- Erdogan F, Ratwani M (1972) A circumferential crack in a cylindrical shell under torsion. *Int J Fract Mech* 8:87–95
- Feaugas X, Clavel M (1997) Cyclic deformation behaviour of an alpha/beta titanium alloy. 1. Micromechanisms of plasticity under various loading paths. *Acta Materialia* 45:2685–2701
- Feng M, Ding F, Jiang Y (2006) A study of loading path influence on fatigue crack growth under combined loading. *Int J Fatigue* 28:19–27
- Findley WN (1957) Fatigue of metals under combination of stresses. *Trans ASME* 79:1337–1348
- Gao H, Brown MW, Miller KJ (1983) Fatigue crack growth under non-proportional loading. In: Proceedings of the international symposium on fracture (ICF), Beijing 22–25 Nov 1983, Science Press, China, pp 666–671
- Hourlier F, d'Hondt H, Truchon M, Pineau A (1985) In: Miller KJ, Brown MW (eds) *Multiaxial fatigue*. ASTM STP 853. ASTM, Philadelphia, pp 228–248
- Otsuka A, Mori K, Togho K (1987) Mode II fatigue crack growth in aluminium alloys. In: *Current research on fatigue cracks, current Japanese materials research*, vol 1. Elsevier, London, pp 149–180
- Pinna C, Doquet V (1999) The preferred fatigue crack propagation mode in a M250 maraging steel loaded in shear. *Fatigue Fract Eng Mater Struct* 22:173–183
- Planck R, Kuhn G (1999) Fatigue crack propagation under non-proportional mixed-mode loading. *Eng Fract Mech* 62:203–229
- Smith KN, Watson P, Topper TH (1970) A stress–strain function for the fatigue of metals. *J Mater* 5:767–778
- Stanzl S, Czegley M, Mayer HR, Tschegg E (1989) Fatigue crack growth under combined Mode I and Mode II loading. In: Wei RP, Gangloff RP (eds) *Fracture mechanics: perspectives and directions*, ASTM STP 1020. ASTM, Philadelphia, pp 479–496
- Tong J, Yates JR, Brown MW (1995) A model for sliding mode crack closure I & II. *Eng Fract Mech* 52(4):599–623
- Wong SL, Bold PE, Brown MW, Allen RJ (1996) A branch criterion for shallow angled rolling contact fatigue cracks in rails. *Wear* 191:45–53
- Wong SL, Bold PE, Brown MW, Allen RJ (2000) Fatigue crack growth rates under sequential mixed-mode I and II loading cycles. *Fatigue Fract Eng Mater Struct* 23:667–674
- You BR, Lee SB (1997) Fatigue crack growth behaviour of SM45C steel under cyclic mode I with superimposed static mode II loadings. *Fatigue Fract Eng Mater Struct* 20(N°7):1059–1074
- Yu X, Abel A (1999) Modelling of crack surface interference under cyclic shear loads. *Fatigue Fract Eng Mater Struct* 22:205–213
- Yu X, Abel A (2000) Fatigue crack growth in notched thin-walled tubes under non-proportional mixed-mode loads, vol IV. In: Proceedings of the 10th Int offshore and polar engineering conference, Seattle, May 28–June 2, 2000, pp 23–28